Ultrasonics 96 (2019) 261–266

Contents lists available at ScienceDirect

Ultrasonics

journal homepage: www.elsevier.com/locate/ultras

Refraction behavior investigation and focusing control of phononic crystals under external magnetic fields

Xiaowei Xue[a], Peng Li[a,b], Feng Jin[a,*]

[a] State Key Laboratory for Strength and Vibration of Mechanical Structures, School of Aerospace, Xi'an Jiaotong University, Xi'an 710049, PR China
[b] School of Human Settlements and Civil Engineering, Xi'an Jiaotong University, Xi'an 710049, PR China

ARTICLE INFO

Keywords:
Negative refraction
Focusing
Equi-frequency surfaces
Ferromagnetic shape memory alloys

ABSTRACT

The refraction and focusing behaviors of two-dimensional phononic crystals (PCs) tuned by external magnetic fields are investigated systematically. The PCs are constructed by inserting ferromagnetic shape memory alloys (FSMAs) between tungsten cylinders and water matrix. Under the magnetic field, material parameters of FSMAs will vary, which furthermore changes the frequency spectrum and equi-frequency surfaces of acoustic waves in sonic crystals. It is revealed that the refraction angle can be tuned from a positive value to a negative one when the PC slab suffers from continuous magnetic fields. Moreover, the focusing behavior can be achieved and controlled artificially by applying a proper magnetic field. These interesting phenomena of the tunable sonic crystals with FSMAs can provide us guidance for the design and application of novel acoustic devices, as well as the active control of acoustic waves.

1. Introduction

During past decades, the physical characteristics of acoustic waves in periodic structures (or phononic crystals simplified as PCs), have attracted tremendous attention [1–6], which shows their potential applications in engineering practice. The priority concerned is the band structures of PCs. If the frequency of acoustic waves locates in the band gap region, their propagation will be prohibited, which can be utilized as acoustic filters or noise control [7–9]. Besides, if the frequency corresponds to some band branch, PCs can exhibit some anomalous physical phenomena that are not found in nature, such as negative refraction, focusing, collimation, total transmission, cloaking, and so forth [10–12]. Therefore, much efforts and attempts have been centralized and focused on the design and manufacture of PCs, as well as the experimental evidence of these novel phenomena.

Taking negative refraction for instance, two main methods are generally used to realize this phenomenon. The first one is to analyze the equivalent frequency surfaces (EFS) of PCs [13–15], which aims to obtain a negative refraction angle. This investigation methodology originates from negative refractions of electromagnetic waves propagation in left-handed materials with a back wave effect (i.e., $S \cdot k < 0$, in which S is the Poynting vector, and k is the wave vector) [16]. Owing to the similarity of dynamic governing equations between electromagnetic and acoustic waves, an analogical method from electromagnetics can be expanded and applied into acoustics directly. The other one is the proper structural design using the concept of meta-surface. According to the generalized Snell law, the phase of acoustic waves can be manipulated arbitrarily, which has the ability to control the wave propagation and realize the negative refraction [17–20].

To date, most PCs and metamaterials are passive and hardly adjustable once fabricated, which is not suitable for practical engineering applications. One of the most significant challenges in PCs development is to explore their flexibility and realize the ability to tune their performance without structural modifications [21]. It is highly desired to design a kind of tunable PCs, especially for the active control of wave refraction [22,23]. Introducing the dielectric elastomer into PCs is an efficient way to control wave propagation, such as the work by Yang et al [24]. Under external electric field, the deformation of the dielectric elastomer changes evidently; and thus the corresponding band structures shift. Hence, it is convenient to alter different electric fields on PCs according to specific engineering requirements. Besides, an adaptive PC to modulate refracted waves has been fabricated, which contains arrayed piezoelectric units with individually connected capacitance elements [25,26]. Therefore, the wave propagation can be tuned via external circuits, which is portable and controllable.

Motivated by these modulation styles, a tunable PC, consisting of ferromagnetic shape memory alloys (FSMAs), is designed and illustrated in this paper, aiming at controlling the wave refraction actively and manipulating focusing behaviors arbitrarily. After a systematic investigation of EFS, both the tunable negative refraction and focusing

* Corresponding author.
E-mail address: jinfengzhao@263.net (F. Jin).

https://doi.org/10.1016/j.ultras.2018.12.007
Received 18 August 2018; Received in revised form 24 November 2018; Accepted 12 December 2018
Available online 13 December 2018
0041-624X/

are shown under different conditions. For a given demand for wave propagation, it is satisfactory to apply specific magnetic field on FSMAs only, without changing geometrical parameters of PCs. Indeed, the final engineering application of this composite structure is not easy. However, the scientific research in this paper is still valuable, because it can provide us a new methodology to manipulate acoustic waves. Additionally, the whole PC is steerable and can be utilized repeatedly, which is easy for the future application.

2. Model description

The two-dimensional (2D) PC, consisting of the FSMAs-coated tungsten cylinders in square lattice immersed in water matrix, is shown in Fig. 1(a). The inner and outer radiuses of the coating layer are respectively $r_b = 0.3825a$ and $r_a = 0.45a$ with the lattice constant $a = 0.1$ m. Considering that the height of the composites is much larger than the section size, it can be degenerated into a two-dimensional plane strain problem. An external magnetic field H_e is imposed in the horizontal plane, and meanwhile the pre-stress σ_0 along z-axis is also considered, such as Fig. 1(b).

Under external stimulus, the material parameters of FSMAs, especially elastic constants, will be varied, which can be depicted by employing the constitutive relation revealed in Refs. [27–29]. Correspondingly, the generalized strain matrix $\boldsymbol{\varepsilon}$ and magnetic flux density matrix $\boldsymbol{B}$ can be expressed as

$$\begin{aligned}\boldsymbol{\varepsilon} = \langle \mathbf{I} + \xi\{\boldsymbol{L_0} + (\boldsymbol{L_1} - \boldsymbol{L_0})[\boldsymbol{S} - \xi(\boldsymbol{S} - \mathbf{I})]\}^{-1}(\boldsymbol{L_0} - \boldsymbol{L_1})\rangle \boldsymbol{L_0}^{-1}\boldsymbol{\sigma} \\ + \xi\boldsymbol{\varepsilon_r} + \xi(1-\xi)\{\boldsymbol{L_0} + (\boldsymbol{L_1} - \boldsymbol{L_0})[\boldsymbol{S} - \xi(\boldsymbol{S} - \mathbf{I})]\}^{-1}(\boldsymbol{L_0} - \boldsymbol{L}_1)(\boldsymbol{S} - \mathbf{I})\boldsymbol{\varepsilon_r},\end{aligned} \tag{1}$$

$$\boldsymbol{B} = \mu_0(\boldsymbol{M} + \boldsymbol{H}), \tag{2}$$

where $\boldsymbol{\sigma}$, $\boldsymbol{\varepsilon_r}$, $\boldsymbol{L_0}$, $\boldsymbol{L_1}$, $\boldsymbol{S}$ and $\mathbf{I}$ are respectively the generalized stress vector, reoriented strain vector, stiffness matrix of the stress-preferred variant, stiffness matrix of the magnetic field preferred variant, Eshelby tensor, and identity matrix. $\boldsymbol{H}$ and $\boldsymbol{M}$ stand for magnetic field and magnetization vector. μ_0 is vacuum permeability. ξ is the volume fraction of the magnetic field-preferred variant, which is very important for the constitutive equation and can be determined by the kinetic equilibrium equation. Correspondingly, we can get the following equation

$$\begin{aligned}\boldsymbol{\sigma}^{\mathrm{T}}\boldsymbol{\varepsilon_r} + \frac{1}{2}\boldsymbol{\sigma}^{\mathrm{T}}\left(\boldsymbol{\varepsilon}^* + \xi\frac{\partial\boldsymbol{\varepsilon}^*}{\partial\xi}\right) + \mu_0\frac{\partial(\boldsymbol{H}^{\mathrm{T}}\boldsymbol{M})}{\partial\xi} + K\sin^2\theta - \frac{1}{2}\mu_0 N M_s^2\cos^2\theta \\ - \sigma_{tw}\varepsilon_r^{max} = 0.\end{aligned} \tag{3}$$

Here θ, K, N, M_s, σ_{tw}, and $\boldsymbol{\varepsilon}_r^{max}$ are respectively the magnetization rotation angle of the stress-preferred variant, magnetocrystalline anisotropy constant, demagnetizing factor, saturation magnetization, detwinning stress and maximal detwinning strain. The superscript T denotes the transpose. Eqs. (1) and (2) stand for the general constitutive equation of FSMAs, which can be simplified with aid of Eq. (3) in the following form

$$\begin{aligned}\sigma_{ij} &= c_{ijkl}(\boldsymbol{H}, \boldsymbol{\sigma})\varepsilon_{kl} - q_{mij}(\boldsymbol{H}, \boldsymbol{\sigma})H_m, \\ B_n &= q_{nkl}(\boldsymbol{H}, \boldsymbol{\sigma})\varepsilon_{kl} + \mu_{nm}(\boldsymbol{H}, \boldsymbol{\sigma})H_m,\end{aligned} \tag{4}$$

where c_{ijkl}, q_{mij}, and $\boldsymbol{\mu}_{nm}$ are the effective elastic, piezomagnetic, and magnetic permeability constants. The repeated subscript index implies a summation operation. It can be concluded from Eq. (4) that the equivalent elastic constants of FSMAs are affected by the external magnetic field pre-stress. The exhaustive derivation process can be found in Appendix, which is not shown for simplification. After solving dynamic equations with the aid of Bloch boundary conditions, frequency spectrum can be calculated, as well as the quantitative wave speeds under different σ_0 and H_e. For the selected FSMAs for simulation, $M_s = 622$ kA/m, $K = 1.7 \times 10^5$ J m^{-3}, $N = 0.484$, $\mu_0 = 4\pi \times 10^{-7}$ H/m, $E_0 = 2400$ MPa, $E_1 = 400$ MPa, $\upsilon = 0.3$, $\sigma_{tw} = 0.8$ MPa, $\boldsymbol{\varepsilon}_r^{max} = 0.058$ and $\rho = 8300$ kg/m^3 [30]. The pre-stress $\sigma_0 = -0.7$ MPa is fixed during the following simulation process, and the effect of H_e is considered in the present contribution. With the aid of Eq. (1), the elastic constants of FSMAs suffering from the magnetic field are shown in Fig. 2, from which we can conclude that the elastic constants of FSMAs decrease continuously with the increasing of H_e. Especially when the magnetic field locates in the region (307 kA/m, 350 kA/m), the decreasing tendency is very evident. Therefore, it is expected that the wave velocity can be manipulated artificially through the external magnetic field.

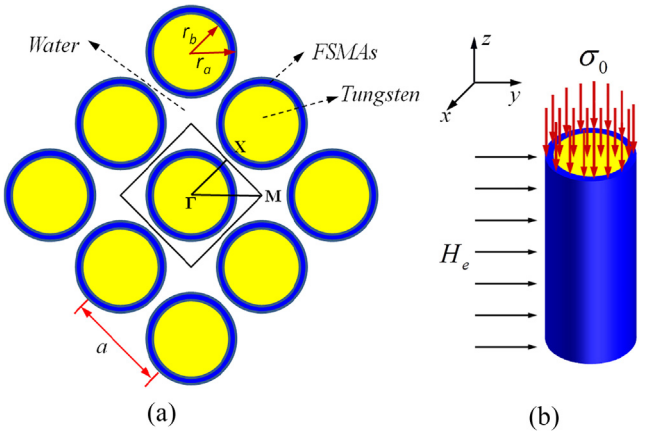

Fig. 1. Schematic diagram of a 2D three-component sonic crystal. (a) the FSMAs-coated tungsten cylinders are arranged in water matrix in the form of square lattice with the inner and outer radiuses of the coating layer respectively r_b and r_a; (b) the unit cell suffering from the external magnetic field H_e and pre-stress σ_0.

3. Results and discussion

The mass density and phase velocities of longitudinal and transverse waves of tungsten cores are as follows: $\rho = 19.3$ g/cm^3, $c_l = 5.09$ km/s, and $c_t = 2.8$ km/s. For water matrix, $\rho_w = 1.0$ g/cm^3 and sound velocity $c = 1.49$ km/s [15]. The following numerical simulations are carried out with the aid of Comsol Multiphysics software. The mesh size is set to be smaller than 1/10 of the shortest wavelength, and recomputations have been done using even finer mesh sizes to ensure the convergence and accuracy of the numerical results.

Fig. 3(a) shows the lowest-order band of the PC along the irreducible Brillouin zone for some selected H_e values. It can be seen from Fig. 3(a) that a larger magnetic field will lead to a smaller phase velocity, which is consistent with Fig. 2 to some extent. Physically, FSMAs can be viewed as a spring, and the tungsten core acts as a rigid mass. Therefore, as the magnetic field increases, the coating layer (FSMAs) will become softened continually, which makes the lowest band shift down.

To qualitatively obtain the group velocity and analyze the refraction routine of acoustic wave incident from water to PCs, mostly, the introduction of EFS is necessary. The EFSs of PCs corresponding to the lowest band of 3500 Hz are deduced from the dispersion curves and plotted in Fig. 3(b), as well as the band structure in water matrix. Here, the red[1] arrows represent the group velocity direction, i.e., energy propagation direction, which coincides with the normal direction to the equi-frequency contour and pointing towards the frequency increment. Essentially, anisotropy of FSMAs under small magnetic fields has negligible effect on the symmetry of equi-frequency contours about Γ-M directions. For example, the black dash dot line with $H_e = 307$ kA/m in Fig. 3(b), exhibits an equi-circle profile, which means small anisotropy.

[1] For interpretation of color in Fig. 3, the reader is referred to the web version of this article.

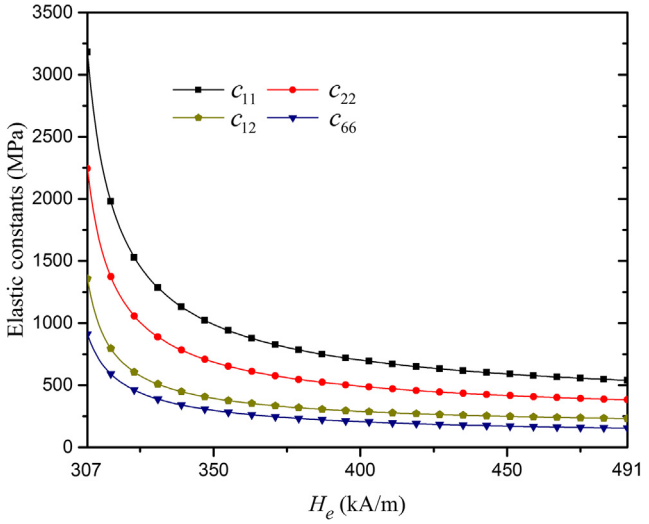

Fig. 2. Variations of the effective elastic constants c_{11}, c_{12}, c_{22} and c_{66} with the magnetic field (The 2D plane strain problem is considered, and hence the variation of other elastic constants is not shown in this figure.)

Meanwhile, if an incident wave with 3500 Hz travels from water to the phononic crystals, it will refract normally, with its propagation path determined by the conservation of the tangential component of the wave vector. However, when the external field increases to 346 kA/m, the equi-frequency branch with the same frequency is nearly quasi-square and becomes convex around M point, with exception of the rounded edges. The incidence and refraction locate on the same side of the interfacial normal direction, which means the so-called negative refraction phenomenon.

In order to prove the correctness of refraction phenomenon mentioned above, a plane wave hitting on the slab consisting of 19 × 39 unit cells with an incident angle of 45° is simulated in the frequency domain, as shown in Fig. 4. In order to avoid the effect of unexpected reflection, wave radiation boundary conditions are used in the outer boundaries of water matrix. When the external magnetic field is relatively small, for example H_e = 307 kA/m in Fig. 4(a), the incident acoustic wave exhibits normal refraction, in accordance with the prediction in Fig. 3(b). However, for a larger magnetic field, such as H_e = 346 kA/m in Fig. 4(b), the evident negative refraction takes place as expected. Overall, the refraction route can be manipulated artificially by the external magnetic field, which provides us a new methodology to control the wave propagation.

After the qualitatively analysis and verification of negative refraction, a quantitative calculation is also necessary for sound wave control. Fig. 5 depicts the dependence of refractive angles on the external magnetic field for different incident angles. Three curves are non-linear, and it is very difficult to exactly express this relation using a simple and general mathematical formula. As the magnetic field increases, the refractive angle decreases monotonously from a positive value, through a negative one, until to −90°. The refractive angles of the PC for the 45° incident wave are respectively 17° at 307 kA/m and −26° at 346 kA/m, which agree with the results in Fig. 4(a). Additionally, the refraction angles are same, all close to 0° when H_e = 323 kA/m, which has no relationship with the incident direction. This critical magnetic field can be considered as the switch between normal refraction and negative refraction. Another critical magnetic field corresponds to the switch between total reflection and negative refraction, i.e., when the refraction angle is –90°. For example, for incident angles of 30°, the corresponding critical field is 442 kA/m. If the external magnetic field is larger than this value, the incident sound wave will reflect totally without refraction. Besides, with the increasing of the incident angle, this critical field corresponding to total reflection becomes smaller, as shown in Fig. 5.

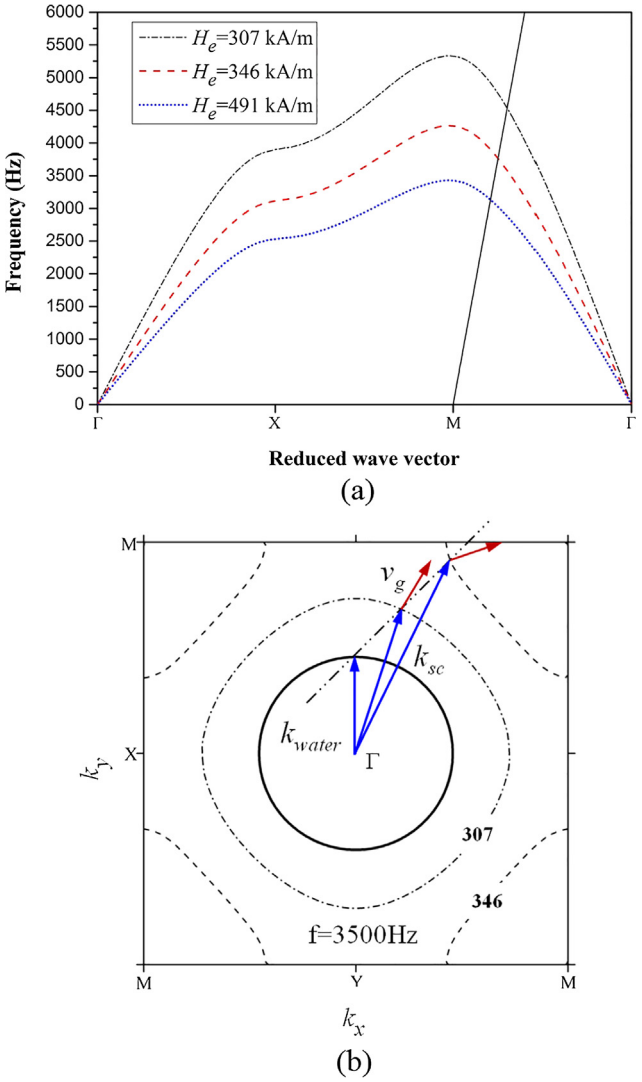

Fig. 3. Theoretical demonstration of the acoustic negative refraction: (a) the band structure of the sonic crystals for different magnetic fields with the straight line beginning at point M representing the dispersion relation of water; (b) EFSs in k space of water (solid line) and PCs with k_{SC} and v_g representing the wave vector and group velocity in the PCs.

The direct application of negative refraction is the implement of wave focusing, in which all angle negative refraction (AANR) is expected. AANR means that negative refraction happens for acoustic waves incident at an arbitrary angle. A straight line beginning at M point, representing the dispersion relation of acoustic waves in water, is added in Fig. 3. The cross point of this line and the band branch determines the upper limit of AANR. It can be seen that as the magnetic field increases, the location of AANR descends, which also dues to the reduction of elastic constants of FSMAs. Briefly, the focusing behaviors of sound waves can be manipulated via different magnetic fields imposed on PCs. In order to prove the tenability of AANR, Fig. 6(a) shows the pressure distribution of the acoustic wave with the frequency 3720 Hz emitted from a point locates when H_e = 346 kA/m. The slab sample with 19 layers thick is chosen, and a wave point source is set at a distance 1.3a from the left surface of the slab. The acoustic wave radiates from the point source, transmits through the slab, and finally focuses into an image on the right side. The distance of the center of the real image point to the right surface of the slab is 12.5a. The full width at half maximum (FWHM) of the image is 0.96 λ with λ representing the wave length of acoustic waves in water. It is smaller than λ, so that the

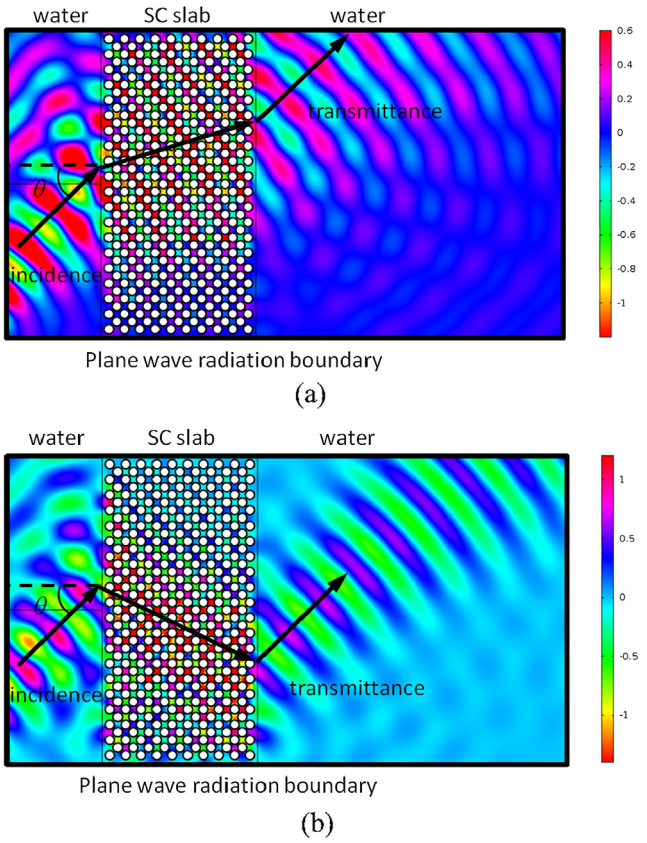

Fig. 4. The pressure field calculated in the frequency domain after a plane wave of 3500 Hz hitting on the slab with an incident angle of 45° for different magnetic fields: (a) 307 kA/m; and (b) 346 kA/m.

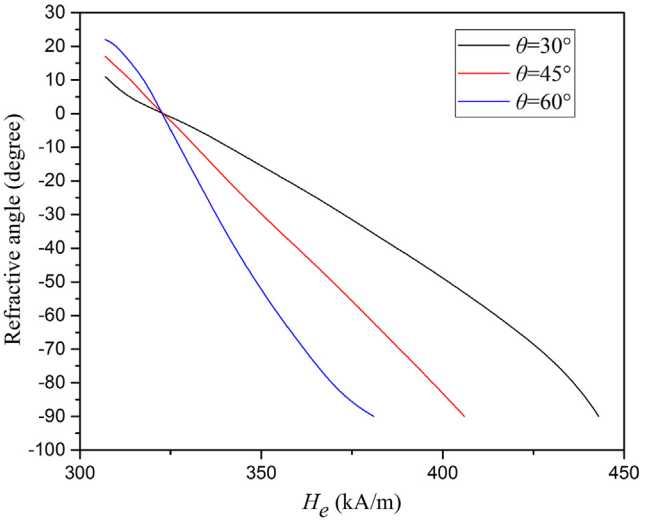

Fig. 5. The dependence of refractive angles on the magnetic field for the incident angles of 30°, 45° and 60° at 3500 Hz.

focusing imaging is satisfactory. By contrast, Fig. 6(b) and (c) respectively depict the pressure distribution under the same conditions when H_e = 307 kA/m and H_e = 491 kA/m. In Fig. 6(b), the acoustic wave exhibits normal refraction, and thus no image can be found in the right. For Fig. 6(c), the incident wave cann't get through the PC slab and almost reflects, which is because the frequency 3720 Hz locates in the band gap when H_e = 491 kA/m.

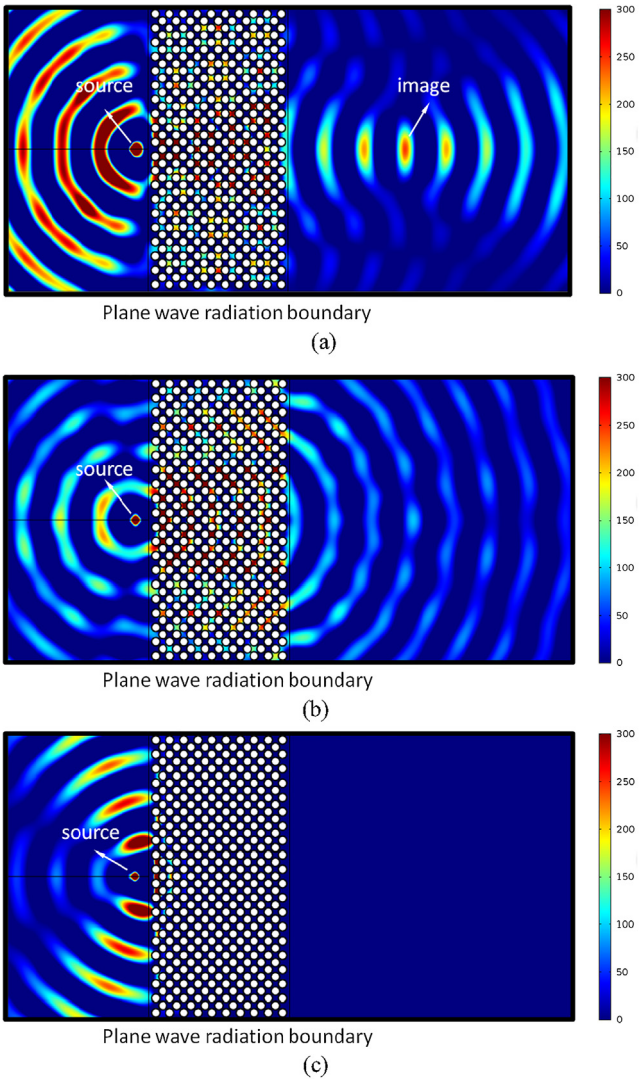

Fig. 6. The pressure field simulations of the tunable PC slab at 3720 Hz with different magnetic fields: (a) H_e = 346 kA/m; (b) H_e = 307 kA/m; and (c) H_e = 491 kA/m.

4. Conclusion

The influence of the external magnetic field in ferromagnetic shape memory alloys on refraction and focusing behaviors of sonic crystals has been illustrated. As a kind of novel smart material, FSMA is used as the coated layer of scatters to artificially manipulate the propagation of the lowest-order acoustic waves. This material exhibits different elastic constants accompanying different external magnetic fields, which is the inner physical mechanism to control wave propagation. It has been revealed that with the increasing magnetic field, the negative refraction phenomenon can be achieved. Meanwhile, the focusing behavior also could be tuned by employing various external magnetic fields. The qualitative findings and quantitative results in this article provide us a new strategy for the design of tunable PCs with negative refraction and focusing behaviors.

Acknowledgment

This research was supported by the National Natural Science Foundation of China (No. 11672223), the Natural Science Foundation of Shaanxi Province (2018JM1039), Project Funded by China Postdoctoral Science Foundation (2018M640975), and Opening Project

from the State Key Laboratory for Strength and Vibration of Mechanical Structures (SV2018-KF-36).

Appendix A

The expressions of effective material constants mentioned above will be given in this section. Different parameters and intermediate variable are listed as matrix for obvious iterative calculation.

$\boldsymbol{M}$, $\boldsymbol{\varepsilon}^*$, θ and $\boldsymbol{\varepsilon_r}$ in Eqs. (1)–(3) can be written as

$$\boldsymbol{M} = \begin{bmatrix} 0 \\ \xi M_s + (1-\xi) M_s \sin\theta \\ (1-\xi) M_s \cos\theta \end{bmatrix}, \tag{A1}$$

$$\boldsymbol{\varepsilon}^* = \{\boldsymbol{L_0} + (\boldsymbol{L_1} - \boldsymbol{L_0})[\boldsymbol{S} - \xi(\boldsymbol{S} - \mathbf{I})]\}^{-1}(\boldsymbol{L_0} - \boldsymbol{L_1})[\boldsymbol{L_0}^{-1}\boldsymbol{\sigma} + (1-\xi)(\boldsymbol{S} - \mathbf{I})\boldsymbol{\varepsilon_r}], \tag{A2}$$

$$\sin\theta = \frac{\mu_0 H_e M_s}{2K + \mu_0 \mathrm{N} M_s^2}, \tag{A3}$$

$$[\boldsymbol{\varepsilon_r}] = \begin{bmatrix} 0 & 0 & 0 \\ 0 & -\varepsilon_r^{\max} & 0 \\ 0 & 0 & \varepsilon_r^{\max} \end{bmatrix} \tag{A4}$$

$\boldsymbol{c}$, $\boldsymbol{q}$, $\boldsymbol{\mu}$ can derived from

$$\begin{aligned} \boldsymbol{c} &= \boldsymbol{s}^{-1}, \\ \boldsymbol{q} &= \boldsymbol{s}^{-1}\boldsymbol{d}, \\ \boldsymbol{\mu} &= \bar{\boldsymbol{\mu}} - \boldsymbol{d}^T\boldsymbol{s}^{-1}\boldsymbol{d}, \end{aligned} \tag{A5}$$

and

$$\begin{aligned} \boldsymbol{s} &= \langle \mathbf{I} + \xi\{\boldsymbol{L_0} + (\boldsymbol{L_1} - \boldsymbol{L_0})\cdot[\boldsymbol{S} - \xi(\boldsymbol{S} - \mathbf{I})]\}^{-1}\cdot(\boldsymbol{L_0} - \boldsymbol{L_1})\rangle\cdot\boldsymbol{L_0}^{-1} + \frac{\partial\boldsymbol{\varepsilon}}{\partial\xi}\cdot\frac{\partial\xi}{\partial\boldsymbol{\sigma}}, \\ \boldsymbol{d} &= \frac{\partial\boldsymbol{\varepsilon}}{\partial\xi}\cdot\frac{\partial\xi}{\partial\boldsymbol{H}}, \\ \bar{\boldsymbol{\mu}} &= \mu_0\left(\frac{\partial\mathbf{M}}{\partial\xi}\cdot\frac{\partial\xi}{\partial\mathbf{H}} + \mathbf{I}\right), \end{aligned} \tag{A6}$$

In addition,

$$\begin{aligned} \frac{\partial\boldsymbol{\varepsilon}^*}{\partial\xi} &= \{\boldsymbol{L_0} + (\boldsymbol{L_1} - \boldsymbol{L_0})\cdot[\boldsymbol{S} - \xi(\boldsymbol{S} - \mathbf{I})]\}^{-1}\cdot(\boldsymbol{L_1} - \boldsymbol{L_0})\cdot(\boldsymbol{S} - \mathbf{I}) \\ &\quad\cdot\{\boldsymbol{L_0} + (\boldsymbol{L_1} - \boldsymbol{L_0})\cdot[\boldsymbol{S} - \xi(\boldsymbol{S} - \mathbf{I})]\}^{-1} \\ &\quad\cdot(\boldsymbol{L_0} - \boldsymbol{L_1})\cdot[\boldsymbol{L_0}^{-1}\cdot\boldsymbol{\sigma} + (1-\xi)(\boldsymbol{S} - \mathbf{I})\cdot\boldsymbol{\varepsilon_r}] \\ &\quad - \{\boldsymbol{L_0} + (\boldsymbol{L_1} - \boldsymbol{L_0})\cdot[\boldsymbol{S} - \xi(\boldsymbol{S} - \mathbf{I})]\}^{-1}\cdot(\boldsymbol{L_0} - \boldsymbol{L_1})\cdot(\boldsymbol{S} - \mathbf{I})\cdot\boldsymbol{\varepsilon_r} \end{aligned} \tag{A7}$$

$$\begin{aligned} \frac{\partial^2\boldsymbol{\varepsilon}^*}{\partial\xi^2} &= 2\{\boldsymbol{L_0} + (\boldsymbol{L_1} - \boldsymbol{L_0})\cdot[\boldsymbol{S} - \xi(\boldsymbol{S} - \mathbf{I})]\}^{-1} \\ &\quad\cdot(\boldsymbol{L_1} - \boldsymbol{L_0})\cdot(\boldsymbol{S} - \mathbf{I})\cdot\{\boldsymbol{L_0} + (\boldsymbol{L_1} - \boldsymbol{L_0})\cdot[\boldsymbol{S} - \xi(\boldsymbol{S} - \mathbf{I})]\}^{-1} \\ &\quad\cdot(\boldsymbol{L_1} - \boldsymbol{L_0})\cdot(\boldsymbol{S} - \mathbf{I})\cdot\{\boldsymbol{L_0} + (\boldsymbol{L_1} - \boldsymbol{L_0})\cdot[\boldsymbol{S} - \xi(\boldsymbol{S} - \mathbf{I})]\}^{-1} \\ &\quad\cdot(\boldsymbol{L_0} - \boldsymbol{L_1})\cdot[\boldsymbol{L_0}^{-1}\cdot\boldsymbol{\sigma} + (1-\xi)\cdot(\boldsymbol{S} - \mathbf{I})\cdot\boldsymbol{\varepsilon_r}] \\ &\quad - 2\{\boldsymbol{L_0} + (\boldsymbol{L_1} - \boldsymbol{L_0})\cdot[\boldsymbol{S} - \xi(\boldsymbol{S} - \mathbf{I})]\}^{-1} \\ &\quad\cdot(\boldsymbol{L_1} - \boldsymbol{L_0})\cdot(\boldsymbol{S} - \mathbf{I})\cdot\{\boldsymbol{L_0} + (\boldsymbol{L_1} - \boldsymbol{L_0})\cdot[\boldsymbol{S} - \xi(\boldsymbol{S} - \mathbf{I})]\}^{-1}\cdot(\boldsymbol{L_0} - \boldsymbol{L_1})\cdot(\boldsymbol{S} - \mathbf{I})\cdot\boldsymbol{\varepsilon_r} \end{aligned} \tag{A8}$$

$$\begin{aligned} \frac{\partial\boldsymbol{\varepsilon}}{\partial\xi} &= \{\boldsymbol{L_0} + (\boldsymbol{L_1} - \boldsymbol{L_0})\cdot[\boldsymbol{S} - \xi(\boldsymbol{S} - \mathbf{I})]\}^{-1}\cdot(\boldsymbol{L_0} - \boldsymbol{L_1})\cdot\boldsymbol{L_0}^{-1}\cdot\boldsymbol{\sigma} \\ &\quad + \xi\{\boldsymbol{L_0} + (\boldsymbol{L_1} - \boldsymbol{L_0})\cdot[\boldsymbol{S} - \xi(\boldsymbol{S} - \mathbf{I})]\}^{-1} \\ &\quad\cdot(\boldsymbol{L_1} - \boldsymbol{L_0})\cdot(\boldsymbol{S} - \mathbf{I})\cdot\{\boldsymbol{L_0} + (\boldsymbol{L_1} - \boldsymbol{L_0})\cdot[\boldsymbol{S} - \xi(\boldsymbol{S} - \mathbf{I})]\}^{-1}\cdot(\boldsymbol{L_0} - \boldsymbol{L_1})\cdot\boldsymbol{L_0}^{-1}\cdot\boldsymbol{\sigma} \\ &\quad + \boldsymbol{\varepsilon_r} + (1-2\xi)\{\boldsymbol{L_0} + (\boldsymbol{L_1} - \boldsymbol{L_0})\cdot[\boldsymbol{S} - \xi(\boldsymbol{S} - \mathbf{I})]\}^{-1}\cdot(\boldsymbol{L_0} - \boldsymbol{L_1})\cdot(\boldsymbol{S} - \mathbf{I})\cdot\boldsymbol{\varepsilon_r} \\ &\quad + \xi(1-\xi)\{\boldsymbol{L_0} + (\boldsymbol{L_1} - \boldsymbol{L_0})\cdot[\boldsymbol{S} - \xi(\boldsymbol{S} - \mathbf{I})]\}^{-1} \\ &\quad\cdot(\boldsymbol{L_1} - \boldsymbol{L_0})\cdot(\boldsymbol{S} - \mathbf{I})\cdot\{\boldsymbol{L_0} + (\boldsymbol{L_1} - \boldsymbol{L_0})\cdot[\boldsymbol{S} - \xi(\boldsymbol{S} - \mathbf{I})]\}^{-1}\cdot(\boldsymbol{L_0} - \boldsymbol{L_1})\cdot(\boldsymbol{S} - \mathbf{I})\cdot\boldsymbol{\varepsilon_r} \end{aligned} \tag{A9}$$

$$\frac{\partial\boldsymbol{M}}{\partial\xi} = \begin{bmatrix} -M_s\cos\theta \\ M_s(1-\sin\theta) \\ 0 \end{bmatrix} \tag{A10}$$

$$\frac{\partial\xi}{\partial\boldsymbol{\sigma}} = -\frac{\boldsymbol{\varepsilon_r}^{\mathrm{T}} + (\boldsymbol{\varepsilon}^*)^{\mathrm{T}} + \xi\left(\frac{\partial\boldsymbol{\varepsilon}^*}{\partial\xi}\right)^{\mathrm{T}}}{\boldsymbol{\sigma}^{\mathrm{T}}\cdot\frac{\partial\boldsymbol{\varepsilon}^*}{\partial\xi} + \frac{1}{2}\xi\boldsymbol{\sigma}^{\mathrm{T}}\cdot\frac{\partial^2\boldsymbol{\varepsilon}^*}{\partial\xi^2}} \tag{A11}$$

$$\frac{\partial \xi}{\partial \boldsymbol{H}} = -\mu_0 \left(\frac{\partial \mathbf{M}}{\partial \xi}\right)^{\mathrm{T}} / \left[\frac{1}{2}\boldsymbol{\sigma}^{\mathrm{T}} \cdot \left(2\frac{\partial \boldsymbol{\varepsilon}^*}{\partial \xi} + \xi \frac{\partial^2 \boldsymbol{\varepsilon}^*}{\partial \xi^2}\right)\right] \tag{A12}$$

References

[1] M.S. Kushwaha, P. Halevi, L. Dobrzynski, B. Djafari-Rouhani, Acoustic band structure of periodic elastic composites, Phys. Rev. Lett. 71 (1993) 2022–2025.
[2] Z. Liu, X. Zhang, Y. Mao, Y.Y. Zhu, Z. Yang, C.T. Chan, P. Sheng, Locally resonant sonic materials, Science 289 (2000) 1734–1736.
[3] C. Goffaux, J. Sanchez-Dehesa, Two-dimensional phononic crystals studied using a variational method: application to lattices of locally resonant materials, Phys. Rev. B 67 (2003) 144301.
[4] M. Maldovan, E.L. Thomas, Simultaneous localization of photons and phonons in two-dimensional periodic structures, Appl. Phys. Lett. 88 (2006) 251907.
[5] P. Li, L. Cheng, Shear horizontal wave propagation in a periodic stubbed plate and its application in rainbow trapping, Ultrasonics 84 (2018) 244–253.
[6] Y. Pennec, B. Djafari-Rouhani, H. Larabi, J.O. Vasseur, A.C. Hladky-Hennion, Low-frequency gaps in a phononic crystal constituted of cylindrical dots deposited on a thin homogeneous plate, Phys. Rev. B 78 (2008) 104105.
[7] R. Martinez-Sala, C. Rubio, L.M. Garcia-Raffi, J.V. Sanchez-Perez, E.A. Sanchez-Perez, J. Llinares, Control of noise by trees arranged like sonic crystals, J. Sound Vib. 291 (2008) 100–106.
[8] S. Benchabane, A. Khelif, A. Choujaa, B. Djafari-Rouhani, V. Laude, Interaction of waveguide and localized modes in a phononic crystal, Europhys. Lett. 71 (2005) 570–575.
[9] Y. Pennec, B. Djafari-Rouhani, J.O. Vasseur, H. Larabi, A. Khelif, A. Choujaa, S. Benchabane, V. Laude, Acoustic channel drop tunneling in a phononic crystal, Appl. Phys. Lett. 87 (2005) 261912.
[10] M. Miguel, D. Chiara, Acoustic metamaterial for subwavelength edge detection, Nat. Commun. 6 (2015) 8037.
[11] J. Shi, S.-C.S. Lin, T.J. Huang, Wide-band acoustic collimating by phononic crystal composites, Appl. Phys. Lett. 92 (2008) 11901.
[12] X. Zhu, B. Liang, W. Kan, X. Zou, J. Cheng, Acoustic cloaking by a superlens with single-negative materials, Phys. Rev. Lett. 106 (2011) 014301.
[13] F. Cervera, L. Sanchis, J.V. Sánchez-Pérez, R. Martínez-Sala, C. Rubio, F. Meseguer, C. López, D. Caballero, J. Sánchez-Dehesa, Refractive acoustic devices for airborne sound, Phys. Rev. Lett. 88 (2002) 023902.
[14] C. Qiu, X. Zhang, Z. Liu, Far-field imaging of acoustic waves by a two-dimensional sonic crystal, Phys. Rev. B 71 (2005) 054302.
[15] J. Li, Z. Liu, C. Qiu, Negative refraction imaging of acoustic waves by a two-dimensional three-component phononic crystal, Phys. Rev. B 73 (2006) 054302.
[16] V.G. Veselago, The electrodynamics of substances with simultaneously negative values of ε and μ, Sov. Phys. Usp. 10 (1968) 509–514.
[17] K. Tang, C. Qiu, M. Ke, J. Lu, Y. Ye, Z. Liu, Anomalous refraction of airborne sound through ultrathin metasurfaces, Sci. Rep. 4 (2014) 6517.
[18] Y. Xie, W. Wang, H. Chen, A. Konneker, B.-I. Popa, S.A. Cummer, Wavefront modulation and subwavelength diffractive acoustics with an acoustic metasurface, Nat. Commun. 5 (2014) 5553.
[19] B. Yuan, Y. Cheng, X. Liu, Conversion of sound radiation pattern via gradient acoustic metasurface with space-coiling structure, Appl. Phys. Express. 8 (2015) 027301.
[20] L. Cao, Z. Yang, Y. Xu, Steering elastic SH waves in an anomalous way by metasurface, J. Sound. Vib. 418 (2018) 1–14.
[21] W.-P. Yang, L.-W. Chen, The tunable acoustic band gaps of two-dimensional phononic crystals with a dielectric elastomer cylindrical actuator, Smart Mater. Struct. 17 (2008) 01501.
[22] L. Feng, X.-P. Liu, M.-H. Lu, Y.-B. Chen, Y.-F. Chen, Y.-W. Mao, J. Zi, Y.-Y. Zhu, S.-N. Zhu, N.-B. Ming, Refraction control of acoustic waves in a square-rod-constructed tunable sonic crystal, Phys. Rev. B 73 (2006) 193101.
[23] L.-Y. Wu, L.-W. Chen, The dispersion characteristics of sonic crystals consisting of elliptic cylinders, J. Phys. D 40 (2007) 7579–7583.
[24] W.-P. Yang, L.-Y. Wu, L.-W. Chen, Refractive and focusing behaviours of tunable sonic crystals with dielectric elastomer cylindrical actuators, J. Phys. D 41 (2008) 135408.
[25] J. Xu, J. Tang, Tunable prism based on piezoelectric metamaterial for acoustic beam steering, Appl. Phys. Lett. 110 (2017) 181902.
[26] Y. Chen, G. Hu, G. Huang, A hybrid elastic metamaterial with negative mass density and tunable bending stiffness, J. Mech. Phys. Solids. 105 (2017) 179–198.
[27] N.N. Sarawate, M.J. Dapino, A continuum thermodynamics model for the sensing effect in ferromagnetic shape memory Ni–Mn–Ga, J. Appl. Phys. 101 (2007) 123522.
[28] X. Wang, F. Li, A kinetics model for martensite variants rearrangement in ferromagnetic shape memory alloys, J. Appl. Phys. 108 (2010) 113921.
[29] X. Wang, F. Li, Variation of magnetic domain structure during martensite variants rearrangement in ferromagnetic shape memory alloys, Appl. Phys. Lett. 101 (2012) 032401.
[30] N. Sarawate, M. Dapino, Variation of magnetic domain structure during martensite variants rearrangement in ferromagnetic shape memory alloys, Appl. Phys. Lett. 88 (2006) 121923.